

Microstresses in particulate-reinforced brittle composites

DEAN-MO LIU

Department of Metals and Materials Engineering, University of British Columbia, 309-6350 Stores Road, Vancouver, BC, Canada V6T 1Z4

E. JENNY WINN

Department of Materials Science and Engineering, University of Pennsylvania, 3231 Walnut Street, Philadelphia, PA19104-6272, USA

The magnitude and spatial distribution of internal microstresses, arising from thermal expansion mismatches, in particulate-reinforced brittle composites were analyzed theoretically using a concentric sphere model. The extent of the stress interaction between inclusions was found to be strongly related to the inclusion size and content, and correspondingly had a considerable effect on the strain energy stored by the matrix. Taking the effect of stress interaction into account, the critical inclusion size for spontaneous microcracking was evaluated, and was found to be a function of the inclusion content.

© 2001 Kluwer Academic Publishers

1. Introduction

The development of composite materials has provided promising properties that are attractive for advanced applications. For those composites having one ductile component, where the stored strain energy can be easily relieved by plastic deformation, considerable internal stresses can still arise on cooling from the fabrication temperature, where the stresses can result at temperature below which the ductility can no longer occur to relieve them. These are mostly due to the mismatch in the coefficient of thermal expansion (CTE), in addition to elastic modulus differences, between the components of the ceramic matrix composite [1–3]. The occurrence of internal rupture in brittle composite materials and its influence on material properties have become important subjects in both theoretical and experimental investigations over the last three decades [3–5]. Analysis of the magnitude and distribution of internal stresses due to the introduction of foreign inclusions is well-developed [2, 6, 7], and has concluded that internal fracture appears most likely to originate from inclusions [8, 9]. However, Singh *et al.* [10] indicated that the magnitude of the internal stress is a necessary but not solely sufficient condition for microcracking, and they concluded furthermore that the nature of the multiaxial stress distribution is of significance in the onset of microfracture. Davidge and Green [1] first considered the effect of inclusion size on the formation of microcracks in brittle composites and found that a minimum dispersion size is essentially required for internal rupture to occur. However, most studies concerning the internal stresses in brittle composites originate from the consideration of a single particle (generally of a spherical shape) embedded in an infinite isotropic matrix. This theory holds only for composites with a sufficiently

low second-phase particle content. Any extension of the theory in describing the characteristics of internal stresses in brittle composites with higher inclusion contents may lead to appreciable errors. Therefore a model, which was first proposed by Aahmy *et al.* [11] and resulted in excellent prediction of the thermal expansion behavior of composites, based on one sphere fitted into another spherical shell with an internal stress balance at the inclusion-matrix interface was used in this study. The internal stress interaction was considered and the critical inclusion size for spontaneous microcracking evaluated. The minimum inclusion content, i.e. critical content, was also determined.

2. Concentric sphere model

The model proposed by Aahmy *et al.* for thermal expansion predictions in two-phase composites considers a stress balance between a sphere of radius a and a surrounding spherical shell of inner radius a and outer radius b , as shown in Fig. 1. If both solids are in perfect contact the balance stress (σ_a) at the interface is given by

$$\sigma_a = \frac{-(\alpha_i - \alpha_m)T}{\frac{2a^3(1 - 2\nu_m) + b^3(1 + \nu_m)}{2E_m(b^3 - a^3)} + \frac{1 - 2\nu_i}{E_i}} \quad (1)$$

where the inner sphere (representing the inclusion) has elastic properties E_i and ν_i and a CTE α_i and the outer shell (the matrix phase) has the properties E_m , ν_m and α_m respectively.

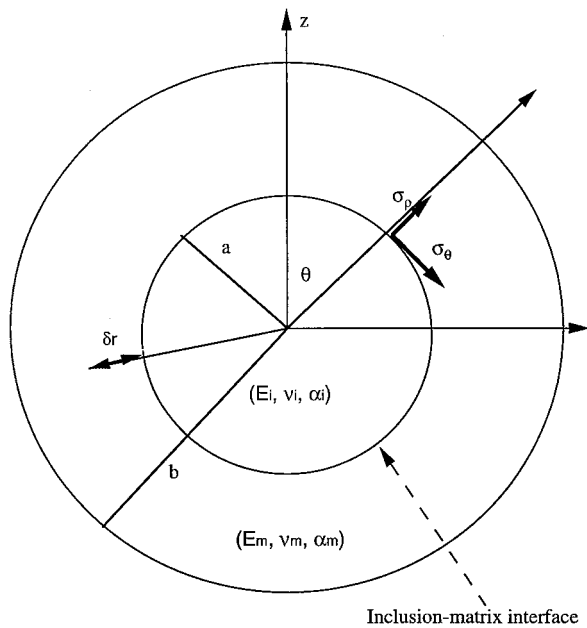


Figure 1 Concentric sphere model.

Considering the stresses acting on the inner shell: using elasticity theory, it can be shown that the radial and tangential components of the stress (σ_ρ and σ_θ respectively), at a distance r from the center of the sphere, can be expressed in a polar coordinate system (see Fig. 1) as given by Equations 2 and 3.

$$\sigma_\rho = \sigma_a \frac{a^3(b^3 - r^3)}{r^3(a^3 - b^3)} \quad (2)$$

$$\sigma_\theta = -\sigma_a \frac{a^3(2r^3 + b^3)}{2r^3(a^3 - b^3)} \quad (3)$$

The stress σ_α can be either tensile or compressive depending on the relative expansivities of the two solids.

For most ceramic particulate composites, internal stresses arise primarily as a result of the mismatch in CTE (thermal stresses, σ_α) and in elastic properties (elastic stresses, σ_E) on cooling from the fabrication temperatures [12–14]. In the following discussions it is assumed, for simplicity, that the ceramic particulate composites can be considered as an assembly of concentric spheres as envisaged by the Aahmy model.

3. Stress induced by expansion mismatch

Equation 1 can be considered as the internal stress at the particle–matrix interface caused by a thermal expansion mismatch between the two components, with the core sphere representing the included phase. The internal stress σ_α can be either tensile or compressive depending on the relative CTEs of the two solids. If the core material has a higher CTE than the shell, σ_α is tensile (defined as negative) and if the opposite is true σ_α is compressive (defined as positive) relative to the inner surface of the shell.

Substituting Equation 1 into Equations 2 and 3, and using the notation σ_α in place of σ_a , gives radial and tangential stresses:

$$(\sigma_\alpha)_\rho = \frac{-(\alpha_i - \alpha_m)T}{\frac{2a^3(1 - 2\nu_m) + b^3(1 + \nu_m)}{2E_m(b^3 - a^3)} + \frac{1 - 2\nu_i}{E_i}} \times \frac{a^3(b^3 - r^3)}{r^3(a^3 - b^3)} \quad (4)$$

$$(\sigma_\alpha)_\theta = \frac{(\alpha_i - \alpha_m)T}{\frac{2a^3(1 - 2\nu_m) + b^3(1 + \nu_m)}{2E_m(b^3 - a^3)} + \frac{1 - 2\nu_i}{E_i}} \times \frac{a^3(2r^3 + b^3)}{2r^3(a^3 - b^3)} \quad (5)$$

Since the composite is assumed to be an assembly of concentric spheres of various sizes, the cube of the ratio of the core radius (a) to that of the outer shell (b) corresponds to the volume fraction of inclusions, denoted as $x (= \{a/b\}^3)$. Thus, after rearrangement, Equations 4 and 5 can be rewritten as functions of the size and content of the included phase;

$$(\sigma_\alpha)_\rho = \frac{-(\alpha_i - \alpha_m)T}{\frac{2x(1 - 2\nu_m) + (1 + \nu_m)}{2E_m(1 - x)} + \frac{1 - 2\nu_i}{E_i}} \times \frac{\left(\frac{a}{a + \delta r}\right)^3 - x}{x - 1} \quad (6)$$

$$(\sigma_\alpha)_\theta = \frac{(\alpha_i - \alpha_m)T}{\frac{2x(1 - 2\nu_m) + (1 + \nu_m)}{2E_m(1 - x)} + \frac{1 - 2\nu_i}{E_i}} \times \frac{\frac{a^3}{x(a + \delta r)^3} + 2}{2\left(1 - \frac{1}{x}\right)} \quad (7)$$

where δr is a distance from particle–matrix interface, i.e. $r = a + \delta r$. For a spherical inclusion embedded in an infinite matrix, where $x \approx 0$, Equations 6 and 7 would result in the same expressions as those derived by Selsing [2]. Selsing’s derivation, which is the relationship most frequently used in the literature, is an extreme case of the above equations and provides only limited information about the internal stresses. Use of Selsing’s equation for investigation of the nature of internal stresses in composites with appreciable fractions of second-phase inclusions is likely to lead to an appreciable error.

The stresses at the particle–matrix interface, i.e. $\delta r = 0$ given by Equations 6 and 7 depend strongly upon the inclusion content. For a fixed fraction of inclusions, both stresses at a distance δr increase with the size of the inclusion. This is consistent with those stresses first observed by Davidge and Green in a glass-thoria composite system [1].

If the inclusion size is sufficiently small compared with the dimensions of the surrounding phase, or if the system is dilute with only a small fraction of inclusions, then we can obtain simplified relationships by setting $b \gg a$ or $(1 - (b^3/a^3)) \approx -(b^3/a^3)$. Thus Equations 4 and 5 become

$$(\sigma_\alpha)_\rho = \sigma_\alpha x - \left(\frac{a}{a + \delta r} \right)^3 \quad (8)$$

$$(\sigma_\alpha)_\theta = \frac{-\sigma_\alpha}{2} 2x + \left(\frac{a}{a + \delta r} \right)^3 \quad (9)$$

where,

$$\sigma_\alpha = \frac{-(\alpha_i - \alpha_m)T}{\frac{2x(1 - 2\nu_m) + (1 + \nu_m)}{2E_m(1 - x)} + \frac{1 - 2\nu_i}{E_i}}$$

Equations 8 and 9 indicate that both stresses drop off rapidly with the distance from the interface and are valid only for small fractions of inclusions or a small inclusion size. On a cautionary note, the spherical shell model is limited by the assumption that no stress interference occurs at a distance $\delta r = b - a$ [11].

Equations 6 and 7 contain a number of important parameters, including the inclusion content (x), size (a) and distance from the inclusion–matrix interface (δr). It is therefore possible to use simple mathematical treatments to provide an explicit understanding of the ways in which these parameters affect the magnitude and spatial distribution of the thermal stresses.

3.1. Inclusion content effect

Equations 6 and 7 provide a more realistic description of thermal stress behavior than Equations 8 and 9. For the purpose of this analysis a dimensionless parameter, termed the “stress ratio”, is defined as the stress state at a distance (δr) from the inclusion–matrix interface to that at the interface where the maximum stress is developed. A higher value of the stress ratio corresponds to larger internal stresses. Thus, in the radial direction, the stress ratio is

$$\frac{[(\sigma_\alpha)_\rho]_{a+\delta r}}{[(\sigma_\alpha)_\rho]_a} = \frac{\left(\frac{a}{a + \delta r} \right)^3 - x}{1 - x} \quad (10)$$

and in the tangential direction it is given by

$$\frac{[(\sigma_\alpha)_\theta]_{a+\delta r}}{[(\sigma_\alpha)_\theta]_a} = \frac{2 + \frac{1}{x} \left(\frac{a}{a + \delta r} \right)^3}{2 + \frac{1}{x}} \quad (11)$$

By setting $a + \delta r = na$ (where n is an arbitrary number ≥ 1), the variation in stress ratio with distance na from the center of the inclusion can be obtained. Figs 2 and 3 show the radial and the tangential components of the stress ratio, respectively, for several inclusion contents. Both stress ratios display spatial distributions, which decrease rapidly, reaching a plateau within approximately one inclusion radius of the interface (the interface is located at $n = 1$). The negative value of the radial stress component, which appears at higher inclusion contents, suggests a change in the stress state from tension near the interface to compression further

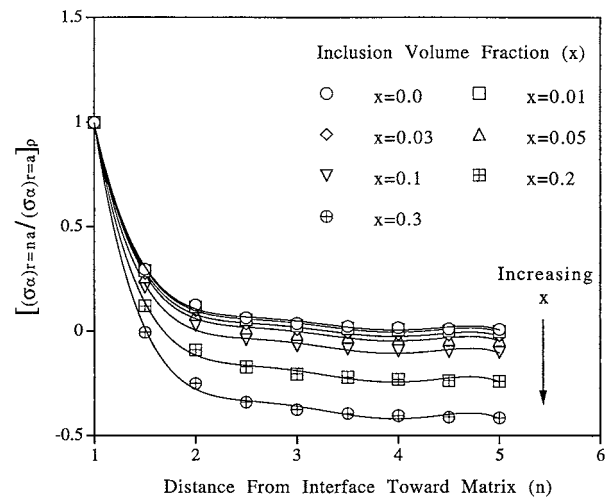


Figure 2 Distribution of radial stress along a line from the interface into the matrix.

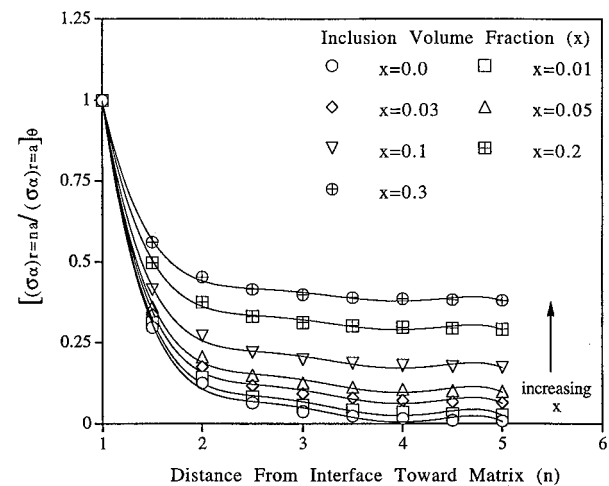


Figure 3 Distribution of tangential stress along a line from the interface into the matrix.

into the matrix, or vice versa depending on the relative magnitudes of α_i and α_m . However, this variation in stress state is absent in the tangential component. More interestingly, at any fixed distance from the interface, the stress components demonstrate the opposite dependence upon inclusion content; an increased inclusion content decreased the radial stress ratio but increased the ratio in the tangential direction. The actual reason is not clear at present, but this finding strongly suggests the existence of stress interactions between inclusions. This stress interaction between neighboring inclusions should provide crucial role in dominating final stress distribution within the composites and will be discussed in detail below.

Consider two contacting model spheres containing inclusions, designated A and B, as shown in Fig. 4: each of which has the same structure as that depicted in Fig. 1. At any distance δr from the interface, the magnitude and spatial distribution of the stress can be approximated by a linear combination of the stresses due to the two nearest spheres because they interfere most strongly. Hence, the combined radial stress is obtained by using the stress ratio defined in Equation 10:

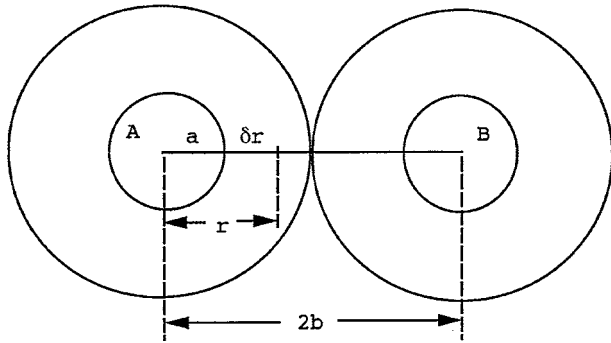


Figure 4 Two adjacent concentric spheres with the same structure as that in Fig. 1.

$$\frac{[(\sigma_\alpha)_\rho]_{a+\delta r}}{[(\sigma_\alpha)_\rho]_a} = \frac{\left(\frac{a}{r}\right)^3 - \left(\frac{a}{2b-r}\right)^3}{1-x} \quad (12a)$$

and in the tangential direction, the combined stress ratio is given by

$$\frac{[(\sigma_\alpha)_\theta]_{a+\delta r}}{[(\sigma_\alpha)_\theta]_a} = \frac{\frac{1}{x}\left(\frac{a}{r}\right)^3 + \left(\frac{a}{2b-r}\right)^3 + 4}{2 + \left(\frac{1}{x}\right)} \quad (13a)$$

The factor of $a/(2b-r)$ in Equations 12a and 13a is the stress contributed by the nearest inclusion, which was assumed to be the one that interacted most strongly. The term $2b$ is defined as the interparticle (center-to-center) separation and can be expressed as

$$\lambda = \frac{D}{x^{1/3}} \quad (14)$$

where $\lambda = 2b$ and the inclusion size $D = 2a$. For simplicity, the distance r is expressed as a multiple (n) of the inclusion radius, i.e. na , where n is an arbitrary number ≥ 1 . Substituting r and Equation 14 into Equations 12a and 13a yields,

$$\frac{[(\sigma_\alpha)_\rho]_{a+\delta r}}{[(\sigma_\alpha)_\rho]_a} = \frac{(n)^{-3} - \left(\frac{2}{x^{1/3} - n}\right)^{-3}}{1-x} \quad (12b)$$

$$\frac{[(\sigma_\alpha)_\theta]_{a+\delta r}}{[(\sigma_\alpha)_\theta]_a} = \frac{\frac{1}{x}n^{-3} + \left(\frac{2}{x^{1/3} - n}\right)^{-3} + 4}{2 + \frac{1}{x}} \quad (13b)$$

Both combined stress ratios are independent of inclusion size but depend strongly on the inclusion content. Figs 5 and 6 illustrate the radial and tangential components of the combined stress for various inclusion contents, plotted as a function of the relative position along a line joining the two inclusion centers. Both combined stresses are symmetric about the point midway (denoted as 0) between the two inclusions.

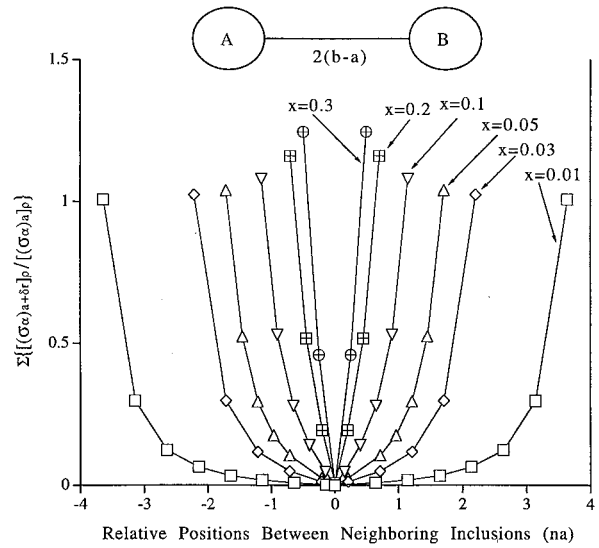


Figure 5 Spatial Distribution of radial stress between two adjacent inclusions.

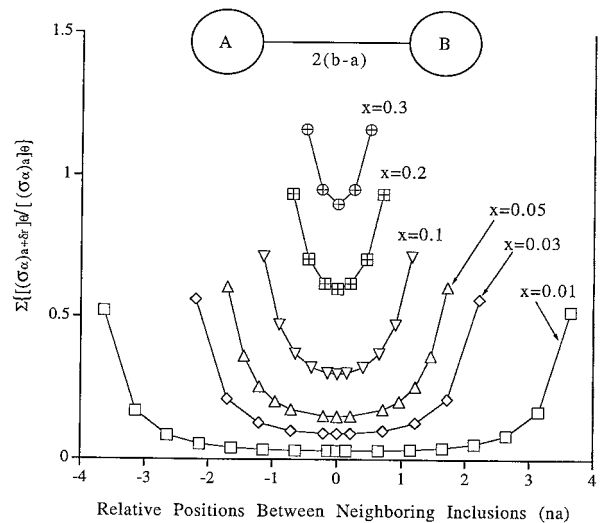


Figure 6 Spatial Distribution of tangential stress between two adjacent inclusions.

Considering first the radial component (Fig. 5); with an increased inclusion content (x) the interfacial distance between inclusions ($2b-2a$) is decreased, and is accompanied by an increased interfacial stress ratio. All the curves of stress ratio decrease sharply to a minimum value at the midpoint, at which position the magnitude of the stress ratio increases with inclusion content (the values are too small to be clearly identified in Fig. 5, but are always non-zero). The radial stress distribution between inclusions becomes sharper for higher contents than for lower ones. These observations indicate that the radial stresses do interact with each other but that the effect is actually rather small because the “effective distance” for such radial stresses is rather short, being only about 1 to 2 times the inclusion radius. On the contrary, the magnitude and distribution of the combined tangential stresses, depicted in Fig. 6, are rather different from those in the radial direction. There is an obvious interaction effect between inclusions, even at the central position where the magnitude of the stress ratio increases with an increased inclusion content. Comparing

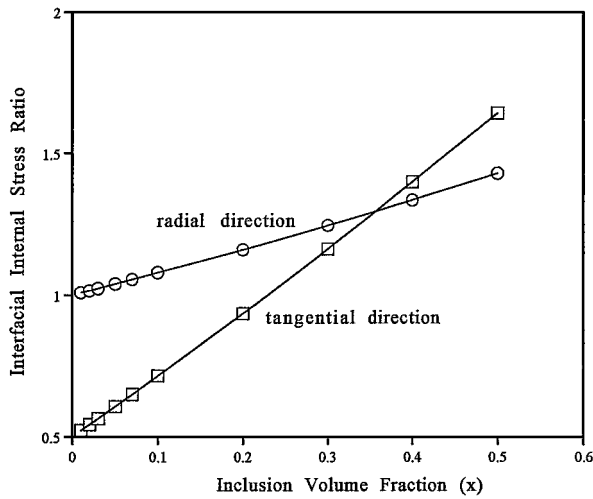


Figure 7 Radial and tangential components of the interfacial stress ratio at various inclusion contents.

the stress ratios at the inclusion–matrix interface (i.e. at $n = 1$) for various inclusion contents, as shown in Fig. 7, it can be seen that the interfacial stress in both directions is approximately linearly proportional to the inclusion content.

However there is a higher volume fraction dependence in the tangential direction than in the radial direction. This gives rise to the presence of stronger interfacial tangential stresses than interfacial radial stresses when the inclusion content exceeds approximately 0.35. This finding may prove important for enhancing the fracture toughness of composite materials [16, 17] and will be discussed separately.

An evaluation of the magnitude and spatial distribution of internal residual stresses in real materials can now be made by re-writing Equations 6 and 7 in combination with Equations 12a and 13a, which gives,

$$(\sigma_\alpha)_\rho = \frac{-(\alpha_i - \alpha_m)T}{\frac{2x(1 - 2\nu_m) + (1 + \nu_m)}{2E_m(1 - x)} + \frac{1 - 2\nu_i}{E_i}} \times \frac{\left(\frac{a}{r}\right)^3 - \left(\frac{a}{2b - r}\right)^3}{1 - x} \quad (15)$$

$$(\sigma_\alpha)_\theta = \frac{(\alpha_i - \alpha_m)T}{\frac{2x(1 - 2\nu_m) + (1 + \nu_m)}{2E_m(1 - x)} + \frac{1 - 2\nu_i}{E_i}} \times \frac{4 + \frac{1}{x}\left(\frac{a}{r}\right)^3 + \left(\frac{a}{2b - r}\right)^3}{2\left(1 - \frac{1}{x}\right)} \quad (16)$$

3.2. Inclusion size effect

By employing a mathematical treatment similar to that appearing in Section 3.1, the effect of inclusion size on the stress state can be estimated. Taking the original radius a as an unit of distance, setting the size of inclusion to be $R = ma$ (where m is an arbitrary positive number) and then considering a distance δr from the

inclusion–matrix interface allows Equation 10 to be rewritten as

$$\frac{[(\sigma_\alpha)_\rho]_{R+\delta r}}{[(\sigma_\alpha)_\rho]_{a+a}} = \frac{\left(\frac{R}{R + \delta r}\right)^3 - x}{\left(\frac{1}{2}\right)^3 - x} \quad (17)$$

and Equation 11 as

$$\frac{[(\sigma_\alpha)_\theta]_{R+\delta r}}{[(\sigma_\alpha)_\theta]_{a+a}} = \frac{2 + \frac{1}{x}\left(\frac{R}{R + \delta r}\right)^3}{2 + \left(\frac{1}{2}\right)^3 \frac{1}{x}} \quad (18)$$

Both stress ratios, Equations 17 and 18, show a similar dependence upon inclusion size but have an opposing dependence upon inclusion content as illustrated in Figs 8 and 9. A considerable increase in radial stress ratio for $x \geq 0.1$ was observed, and is suggested to be a result of a significant decrease in interparticle spacing. Confirmation of this will follow in a later discussion.

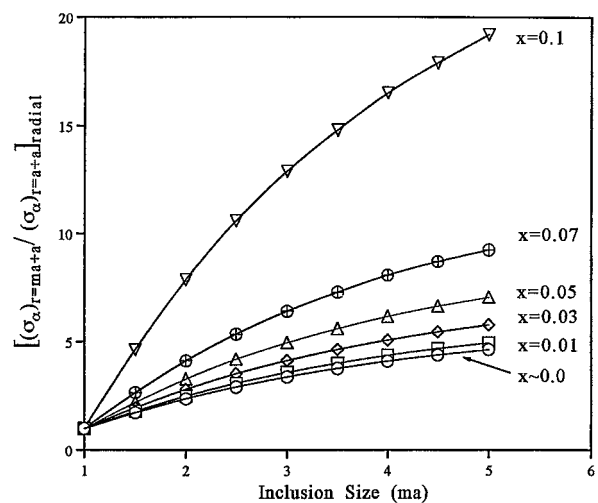


Figure 8 Effect of inclusion size on the radial stress at a fixed distance from the interface, for various inclusion contents.

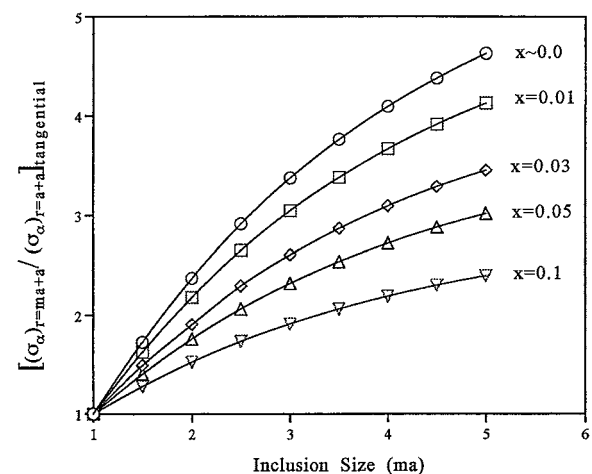


Figure 9 Effect of inclusion size on the tangential stress at a fixed distance from the interface, for various inclusion contents.

Now consider two adjacent model spheres, each of radius R , and set $\delta r = ma$, a distance of m times the unit radius (a). At a distance δr from one of the inclusion-matrix interfaces the radial stress ratio is assumed to be a summation of the stress ratios of the two nearest inclusions and is given by

$$\frac{[(\sigma_\alpha)_\rho]_{R+\delta r}}{[(\sigma_\alpha)_\rho]_R} = \frac{\left(\frac{R}{R+\delta r}\right)^3 - \left(\frac{R}{2Rx^{-1/3} - R - \delta r}\right)^3}{1-x} \quad (19)$$

whilst the combined tangential stress ratio is given by

$$\frac{[(\sigma_\alpha)_\theta]_{R+\delta r}}{[(\sigma_\alpha)_\theta]_R} = \frac{4 + \frac{1}{x} \left(\frac{R}{R+\delta r}\right)^3 + \left(\frac{R}{2Rx^{-1/3} - R - \delta r}\right)^3}{2 + \frac{1}{x}} \quad (20)$$

As an illustration, Figs 10 and 11 respectively show the results for radial and tangential stress ratios at $x = 0.05$. It is interesting to note that the interfacial stress ratio

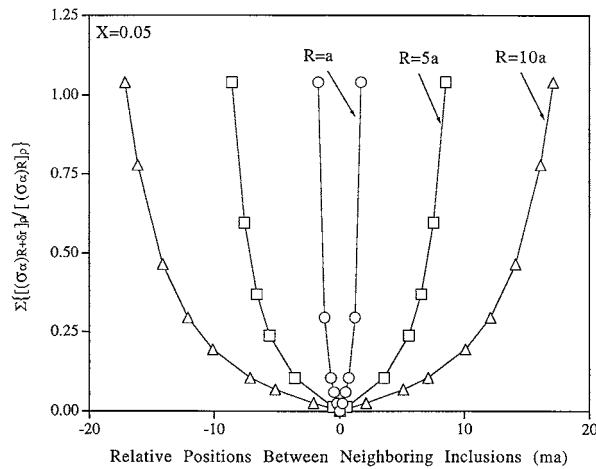


Figure 10 Effect of inclusion size on the spatial distribution of radial stress between two adjacent inclusions at $x = 0.05$.

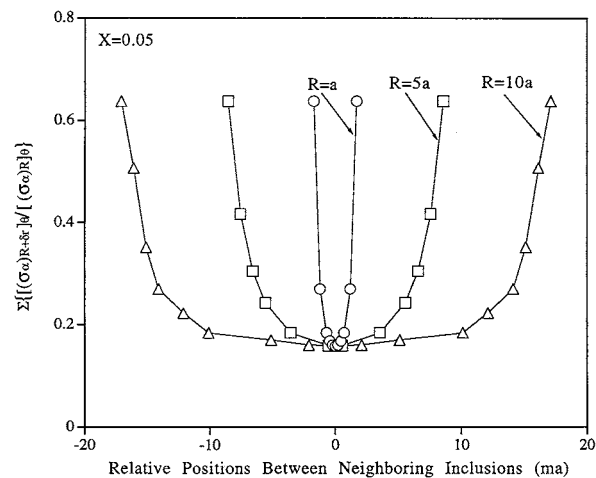


Figure 11 Effect of inclusion size on the spatial distribution of tangential stress between two adjacent inclusions at $x = 0.05$.

is independent of the inclusion size at fixed inclusion content; that is, the interfacial residual stress due to expansion mismatch is independent of the size of the inclusion. The stress ratio (or stress) distribution for various inclusion sizes and contents is quite different; however, the distribution curve is similar in shape, i.e., U shape, and is essentially symmetrical between identical particles. The distribution becomes narrower at lower inclusion contents and smaller inclusion sizes, and conversely it is broader at higher inclusion contents and larger inclusion sizes.

Although Figs 10 and 11 are derived from neighboring spherical inclusions of identical size, it seems conceivable that a certain deformation or shift in the stress ratio—ma profile (U shape) can occur if the neighboring inclusions are different in size. This also implies that the same model can be expanded to account for the effect of particle size distribution; however, is beyond the scope of this work. The shape of the inclusion is also known to affect the stress distribution to a significant extent. However, a successful application of the “idealized” model, as will be discussed later, to a realistic ceramic matrix composites, i.e., $\text{Al}_2\text{O}_3\text{—Cr}_3\text{C}_2$ system, where the inclusions are virtually non-spherical and randomly distributed in particle size, suggests a high feasibility of the “ideal” model to the “real” composite systems.

4. Average internal stresses

In Sections 3.1 and 3.2, the magnitude and distribution of internal residual stresses were obtained in terms of the inclusion content and size, e.g. Figs 5, 6 and Figs 10, 11 respectively. The internal stresses can therefore be estimated by integrating the area under each stress distribution curve. In the radial direction, the integration of Equation 14 gives

$$\int_a^{b-a} \text{Equation 14 } dr = \sigma_\alpha a \frac{1 - (2x^{-1/3} - 1)^{-2}}{1-x} \quad (21)$$

and an average radial stress can be expressed by,

$$\bar{\sigma}_\rho = \sigma_\alpha \frac{1 - (2x^{-1/3} - 1)^{-2}}{(1-x)(x^{-1/3} - 1)} \quad (22)$$

In the tangential direction, the integration of Equation 15 leaves

$$\int_a^{b-a} \text{Equation 15 } dr = \sigma_\alpha a \left[\frac{1 + (2x^{-1/3} - 1)^{-2}}{4(1-x)} \right] \quad (23)$$

giving an average tangential stress of

$$\bar{\sigma}_\theta = \sigma_\alpha \frac{1 + (2x^{-1/3} - 1)^{-2}}{4(1-x)(x^{-1/3} - 1)} \quad (24)$$

where σ_α has been defined previously. Equations 22 and 24 indicate that the average internal stresses are independent of the inclusion size but show a dependence upon the inclusion content. Plotting the average stress

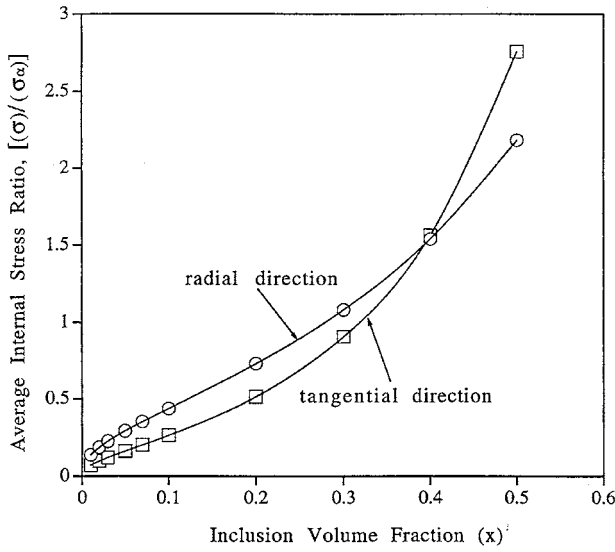


Figure 12 Average internal stress ratio in radial and tangential directions at various inclusion contents.

ratios (defined as $\bar{\sigma}/\sigma_\alpha$ in Equations 22 and 24) with respect to the fraction of inclusions results in a relationship as shown in Fig. 12. This relationship displays a cross-over in the magnitude of the average stresses at an inclusion content of approximate 0.4; below this point the average stress is larger in the radial direction and above this point the average tangential stress is larger. This difference in stress magnitude with inclusion content is important in determining the fracture plane during crack propagation and in suppressing crack extension [5, 16, 18]. Furthermore, the area under each curve is regarded as the stored strain energy. Therefore from Equations 21 and 23, the stored strain energy

energy in the matrix (U_m) subject to orthogonal stresses, σ_ρ , σ_θ and σ_ϕ can be obtained from elasticity theory, giving the total strain energy stored in the matrix [19].

$$U_m = \frac{1}{2E_m}(1 + \nu_m)(\sigma_\rho^2 + \sigma_\theta^2 + \sigma_\phi^2) - \nu_m(\sigma_\rho + \sigma_\theta + \sigma_\phi)^2 \quad (25)$$

Let $\sigma_\theta \approx \sigma_\phi$ and assume this does not introduce a significant error in the estimate of U_m . Substituting for σ_ρ and σ_θ , using Equations 15 and 16 respectively, results however in an integral function which is too tedious to be solved analytically (not shown). Instead, for simplicity and for ease of use, an equation to estimate the critical inclusion size from the average internal stresses, i.e. Equations 22 and 24, was developed. By combining the stored strain energy (U_m) in the matrix, together with the stored strain energy in the inclusion (U_i),

$$U_i = \frac{\sigma_i^2}{2E_i}(1 - 2\nu_i)^2 \quad (26)$$

The critical inclusion size D_c ($=2a_c$, where a_c is defined as the critical radius) for spontaneous microfracture in a semi-spherical geometry can be estimated when the criterion $U_m + U_i >$ fracture energy of composite is met [1]. This gives the relation of,

$$\frac{4}{3}\pi a_c^3(U_m + U_i) > 2\pi a_c^2\gamma_A \quad (27)$$

After rearrangement, the critical inclusion size D_c can be calculated by,

$$D_c > \frac{6\gamma_A}{[(F_\rho^2 + 2F_\theta^2) - 2\nu_m F_\theta(2F_\rho + F_\theta)] \frac{2\sigma_\alpha^2}{E_m} + \frac{\sigma_\alpha^2(1 - 2\nu_i)^2}{E_i}} \quad (28)$$

in each principal direction is proportional to the size of the inclusion. Moreover, the stored strain energy for each principal direction increases with inclusion content and has the same dependence as those observed in Fig. 12.

This stored strain energy–inclusion size relationship explains the phenomenon of spontaneous microcracking which is observed around inclusions of sufficient size. Cracking occurs when the particle size reaches a critical value where the total stored strain energy (i.e. a summation of each stored strain energy component in a three dimensional consideration) exceeds the fracture energy of the composites.

5. Critical inclusion size

In determining the critical inclusion size for spontaneous microcracking due to differential thermal contraction an energy viewpoint is considered to be the most appropriate [1, 5]. Therefore, the stored strain

where

$$F_\rho = \frac{1 - (2x^{-1/3} - 1)^{-2}}{(1 - x)(x^{-1/3} - 1)}$$

$$F_\theta = \frac{1 + (2x^{-1/3} - 1)^{-2}}{4(1 - x)(x^{-1/3} - 1)}$$

and γ_A is the effective fracture energy of the matrix phase, usually taken as $\approx 1 \text{ J/m}^2$. It is important to note that the critical inclusion size (D_c) is strongly related to the inclusion content, which is a frequently-measured experimental parameter [20, 21]. Furthermore, it is possible to estimate a critical volume fraction of second-phase inclusions by using Equation 27 for the onset of microcracking at a given inclusion size.

However, determining the interparticle separation according to Equation 14 may give rise to certain errors since the description of composites as an assembly of concentric spheres of one size only is generally

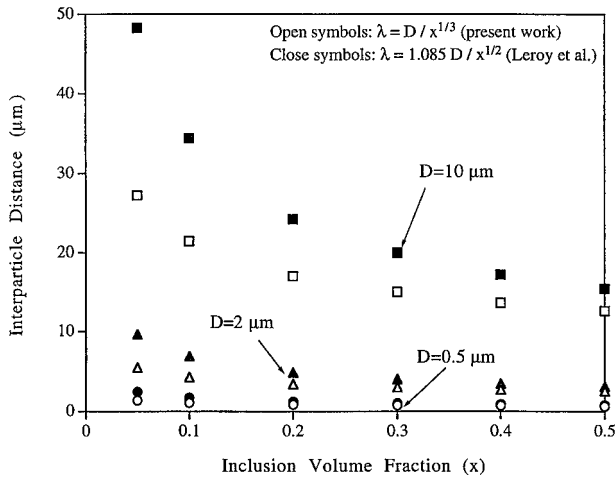


Figure 13 Comparisons of interparticle separation as predicted by Equations 14 and 29.

unrealistic; a more accurate picture would consider an assembly of varying size spheres. Leory *et al.* [22] established experimentally that Equation 14 must be modified statistically to give;

$$\lambda = \frac{1.085D}{x^{1/2}} \quad (29)$$

In fact, both Equations 14 and 29 display similar predictions for \square at small inclusion sizes and high inclusion contents, as depicted in Fig. 13. A substantial deviation occurs for a small concentration of large sized inclusions. The magnitude and spatial distribution of the aforementioned internal stresses, particularly as given by Equations 15 and 16, should be correlated with Equation 29 for real composites. The factors F_{\square} and F_{θ} , in Equation 27, for prediction of the critical inclusion size, should therefore also be approximated by,

$$F_{\rho} = \frac{1 - (2x^{-1/3} - 1)^{-2}}{(1 - x)(1.085x^{-1/2} - 1)}$$

$$F_{\theta} = \frac{1 + (2x^{-1/3} - 1)^{-2}}{4(1 - x)(1.085x^{-1/2} - 1)}$$

Using Equation 28 with factors F'_{\square} and F'_{θ} , Fig. 14 shows experimental observations for $\text{Al}_2\text{O}_3\text{-Cr}_3\text{C}_2$ composites, which have been extensively investigated [21,23]. The figure demonstrates a spontaneous microcracking–inclusion content in good agreement with the predictions of Equation 28. The inset of Fig. 14 also illustrates the predicted results for several ceramic-based particulate composites, such as $\text{Al}_2\text{O}_3\text{-TiC}$, $\text{Al}_2\text{O}_3\text{-Cr}_3\text{C}_2$ and $\text{Si}_3\text{N}_4\text{-SiC}$, which were examined to determine the critical inclusion size for various inclusion contents. The values in parentheses represent the difference in CTE ($\Delta\alpha$) between the inclusion and the matrix phases. The critical inclusion size in brittle composites decreased as the inclusion content increased, with the degree of dependence being strongly related to the differences in elastic constants and CTEs of the components. In fact, it is reasonable to recognize the effect of inclusion content on the critical inclusion size from an energy viewpoint, as substan-

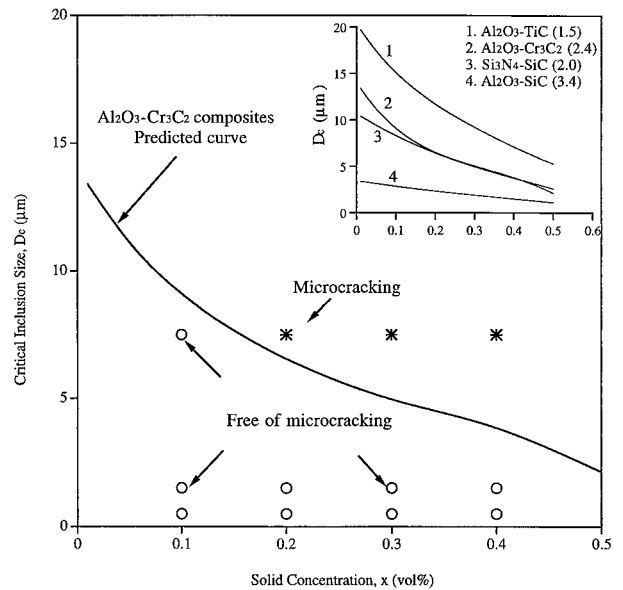


Figure 14 A direct comparison between experimental observation and prediction of the critical inclusion size (Equation 28) in terms of the inclusion content for $\text{Al}_2\text{O}_3\text{-Cr}_3\text{C}_2$ composites, where the sign “X” represents microcracking and “O” shows no sign of microcracking. Inset: prediction of D_c for several ceramic-based particulate composites. (Values in parentheses denote the difference in α).

tiated by Equations 21 and 23 together with Figs 10 and 11.

It is interesting to note that, as previously stated, the prediction for the $\text{Al}_2\text{O}_3\text{-Cr}_3\text{C}_2$ composites is relatively successful, irrespective of the size distribution, shape, and possible clustering effect of the inclusion phase (Cr_3C_2) during sintering. The clustering effect is particularly pronounced when the inclusion concentration is high, for instance, greater than 30 vol%, where some particulate inclusions were found to cluster into large inclusion of complex shape [21]. Since the model proposed is based simply on two concentric spheres of identical size, it is surprised that it provides a reasonably accurate prediction for real composite systems of various inclusion concentration up to 40 vol%, where the size, size distribution, and shape of inclusion phase is far more complicate than that used in the model. This strongly suggests some comprising effect may be present in between which leads to a wide feasibility of the theoretical model proposed here to realistic brittle composite systems.

6. Conclusions

This study provides an alternative way to assess the magnitude and spatial distribution of internal microstresses, arising from CTE mismatches in brittle composites with various contents of second-phase inclusions. Stress interactions between inclusions are an important factor in determining the nature of the stress state and can not be neglected as they are in conventional analyses based on a single particle embedded within an infinite isotropic matrix. The critical inclusion size is strongly influenced by the mismatch in expansivity of the components, the temperature from which the composite is cooled and in particular the inclusion content.

An understanding of the magnitude and distribution of internal stresses between inclusions is of benefit in the prediction of fracture behavior and failure in brittle composites. By considering the nature of internal residual stresses it is expected that improved composites, with good strength and high fracture toughness, can be fabricated.

Acknowledgments

One of authors (DML) gratefully acknowledges the Ministry of Economic Administration, R.O.C. for supporting this research under contract No. 3AB3210. The other author (EJW) is grateful to the US Department of Energy (BES) for support under grand No. DE-FG02-97ER45637-A000, and to the NSF MRSEC program for supporting facilities at the University of Pennsylvania under grand No. DMR96-32598.

References

1. R. W. DAVIDGE and T. J. GREEN, *J. Mater. Sci.* **3** (1968) 629.
2. J. SELSING, *J. Amer. Ceram. Soc.* **44** (1961) 419.
3. W. D. KINGERY, *J. Amer. Ceram. Soc.* **40**(10) (1957) 351.
4. A. G. EVANS, *Acta. Metall.* **26** (1978) 1845.
5. F. F. LANGE, in "Fracture Mechanics of Ceramics, vol. 2," edited by R. C. Bradt, D. P. H. Hasselman, and F. F. Lange (Plenum Press, New York, 1974) p. 599.
6. R. A. CHAPERY, *J. Comp. Mater.* **2**(3) (1968) 380.
7. W. R. BUSSEUM, in "Mechanical Properties of Engineering Ceramics," Chap. 10, edited by W. W. Kriegel and H. Palmour III (Interscience Publishers, New York and London, 1961).
8. A. G. EVANS, *J. Mater. Sci.* **9** (1974) 1145.
9. D. J. GREEN, *J. Amer. Ceram. Soc.* **64**(3) (1981) 138.
10. J. P. SINGH, D. P. H. HASSELMAN, W. M. SU, J. A. RUBIN and R. PALICKA, *J. Mater. Sci.* **16** (1981) 141.
11. A. A. AAHMY and A. N. RAGAI, *J. App. Phys.* **41**(13) (1970) 5108.
12. J. N. GOODIER, *J. App. Mech.* **1**(1) (1933) 39.
13. R. H. EDWARDS, *Trans. AIME* **73**(1) (1951) 19.
14. D. P. H. HASSELMAN and R. M. FULRUTH, *J. Amer. Ceram. Soc.* **50**(8) (1967) 399.
15. T. MORI and K. TANAKA, *Acta. Metall.* **21** (1973) 571.
16. R. A. CUTLER and A. V. VIRKAR, *J. Mater. Sci.* **20** (1985) 3557.
17. R. W. RICE, *Ceram. Eng. Sci. Proc.* **11**(7-8) (1990) 667.
18. M. TAYA, S. HAYASHI, A. S. KOBAYASHI and H. S. YOON, *J. Amer. Cera. Soc.* **71**(12) (1990) 1382.
19. G. E. DIETER, "Mechanical Metallurgy," 2nd ed. (McGraw-Hill Inc., New York, 1976).
20. D. B. BINNS, in "Science of Ceramics," vol.1, edited by G. H. Steward (Academic Press, London, 1962).
21. C. T. FU, J. M. WU and A. K. LI, *J. Mater. Sci.* **29** (1994) 2671.
22. G. LEORY, J. D. EMBURY, G. EDWARDS and M. F. ASHBY, *Acta. Metall.* **29** (1981) 1509.
23. D. M. LIU and C. T. FU, private communication.

*Received 3 May 2000
and accepted 6 February 2001*